Supporting Information

Interphase Formation Versus Fluoride-ion Insertion in Tunnel-Structured Transition Metal Antimonites

Alice R. Giem,[a,b] Jaime R. Ayala,[a,b] Jingxiang Cheng,[a,b] Conan Weiland,[c] Cherno Jaye,[c] Daniel A. Fischer,[c] and Sarbajit Banerjee[a,b] *

[a.] *Department of Chemistry, Texas A&M University, College Station, TX 77843-3012, USA*
[b.] *Department of Material Science and Engineering, Texas A&M University, College Station, TX 77843-3012, USA*
[c.] *Material Measurement Laboratory, National Institute of Standards and Technology, Gaithersburg, MD 20899, USA*
* *Corresponding Authors*

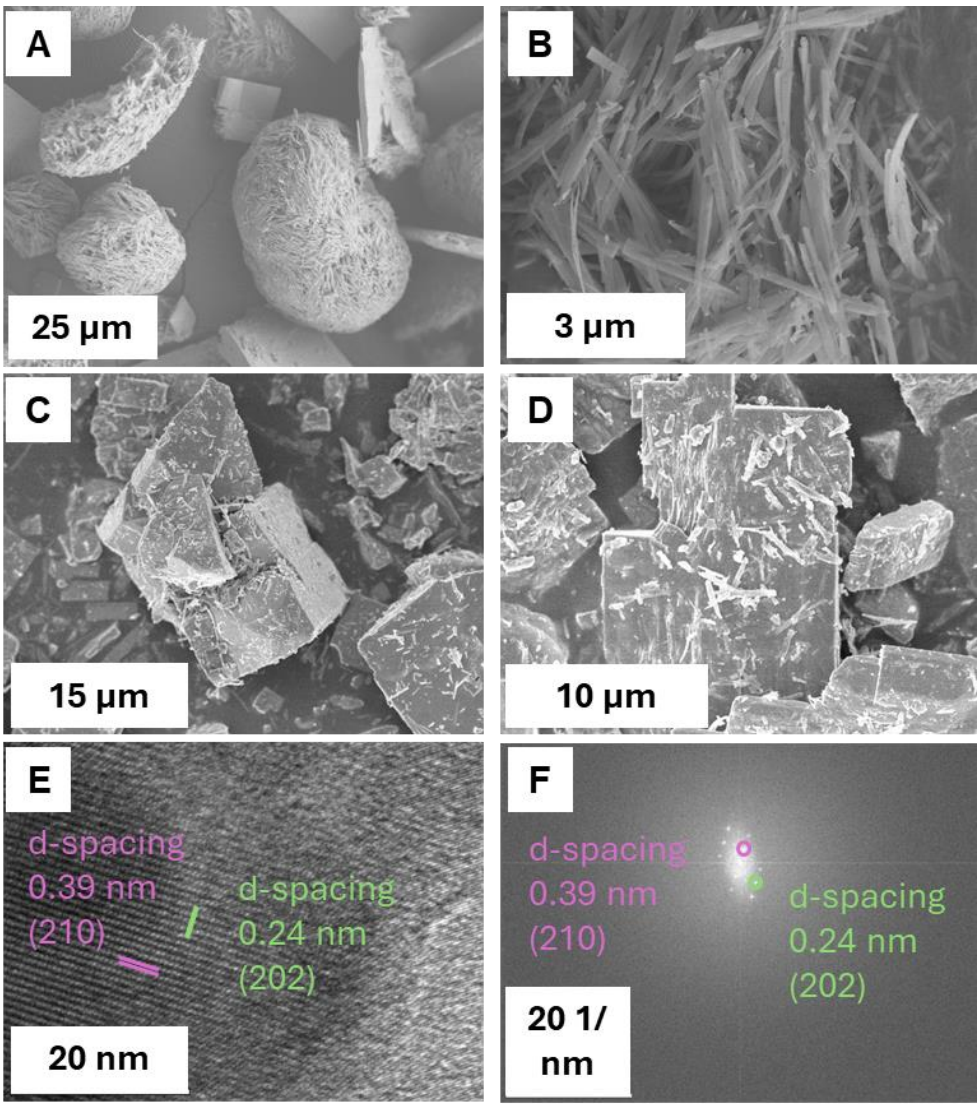

Figure S1. SEM Images of varying magnification for (A) $MnSb_2O_4$ synthesized hydrothermally at low magnification; (B) $MnSb_2O_4$ nanoparticles at higher magnification; (C) $MnSb_2O_4$ after hand grinding with a mortar and pestle; and (D) hand ground $MnSb_2O_4$ after treatment with a 1:1 molar ratio of XeF_2 in CH_3CN at 25 °C. (E) Lattice-resolved HRTEM image acquired for $MnSb_2O_4$ indicating the separation between (210) and (202) planes. (F) Indexed SAED pattern acquired for the as prepared $MnSb_2O_4$ indicating the (210) and (202) planes.

Table S1. Atom positions, fractional occupancies, and thermal parameters obtained from Rietveld refinement of the powder XRD pattern acquired for $MnSb_2O_4$. Refinement statistics and lattice parameters are included in the table header.

a = ***b*** = 8.69572(10) Å, ***c*** = 6.00591(9) Å ***α*** = ***β*** = ***γ*** = 90°; **Volume** = 454.140(10) Å^3 χ^2 = 29.40(3); **wR** = 12.14(2) %; **RF** = 3.29(8) %					
Atom Label	**Site Multiplicity**	***x***	***y***	***z***	**U_{iso} (Å^2)**
Mn	4	0	½	¼	0.0237(7)
Sb	8	0.17858(24)	0.16681(22)	0	0.0165(14)
O(1)	8	0.0961(12)	0.6574(13)	0	0.041(4)
O(2)	8	0.6866(7)	0.1866(7)	¼	0.036(4)

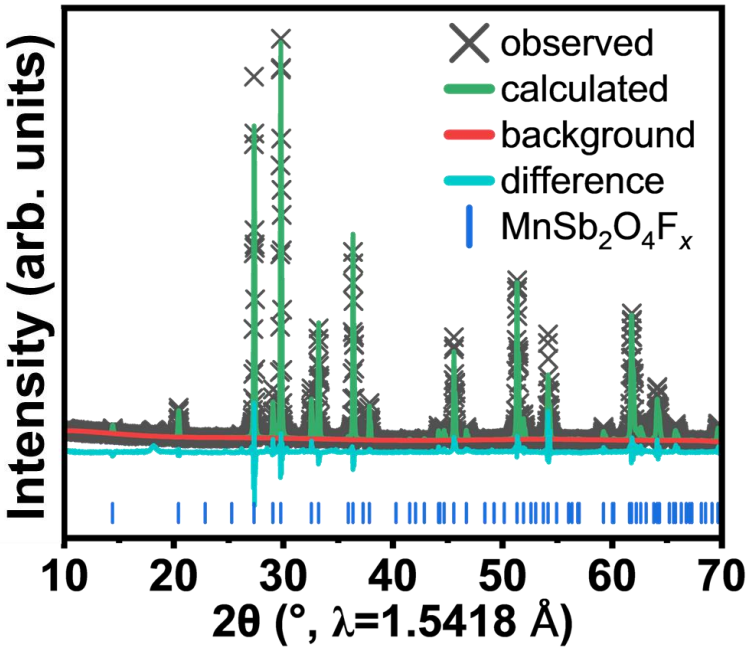

Figure S2. Rietveld refinement of powder X-ray diffraction data collected for $MnSb_2O_4$ after a 1 molar ratio treatment of XeF_2 in CH_3CN. Refinement statistics, lattice parameters, and atom positions for the refinements of the reacted material are shown in Table S2. This material experienced significant preferred orientation (March-Dollase Ratio of 0.527 for the unique axis 0 0 1).

Table S2. Atom positions, fractional occupancies, and thermal parameters obtained from Rietveld refinement of the powder XRD pattern acquired for $MnSb_2O_4$ after treatment with a 1:1 molar ratio of XeF_2 in CH_3CN. Refinement statistics and lattice parameters are included in the table header.

a = ***b*** = 8.69736 Å, ***c*** = 6.00409 Å ***α*** = ***β*** = ***γ*** = 90°; **Volume** = 454.173 Å^3 χ^2 = 10.123; R_{wp} = 12.779%; **RF** = 8.688%					
Atom Label	**Site Multiplicity**	***x***	***y***	***z***	**U_{iso}*100**
Mn	4	0.00	0.50	0.25	0.11(2)
Sb	8	0.1780(1)	0.1684(1)	0.00	0.01(0)
O(1)	8	0.0817(7)	0.6520(3)	0.00	0.22(5)
O(2)	8	0.6754(8)	0.1754(8)	0.25	2.84(1)
F	16	0.5273(5)	0.4961(7)	0.7404(2)	25

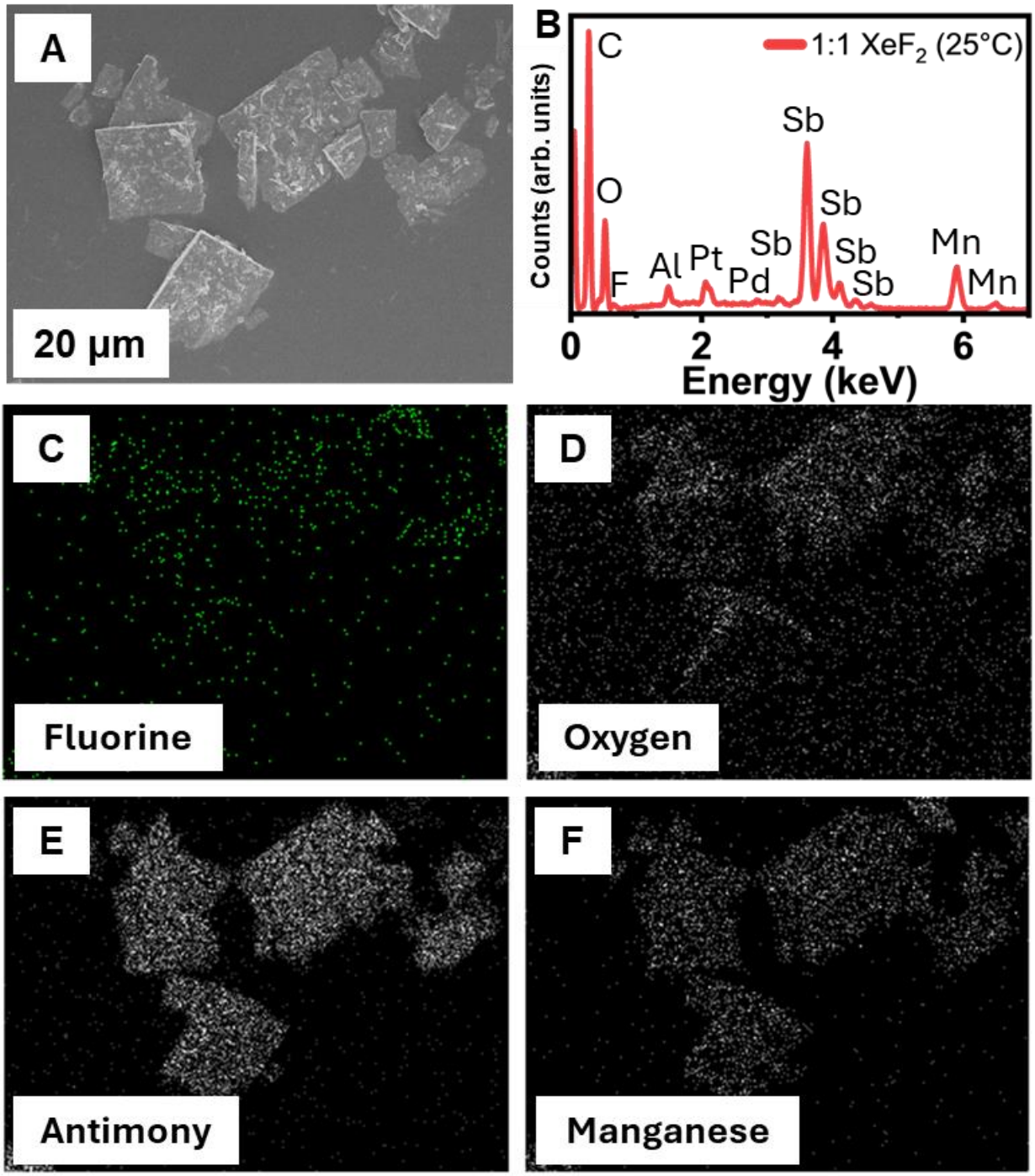

Figure S3. SEM-EDS images of 1:1 molar ratio of XeF_2 in CH_3CN at 25°C with (A) SEM image of as treated $MnSb_2O_4$; (B) EDS spectra; (C) fluorine elemental map; (D) oxygen elemental map; (E) antimony elemental map; and (G) manganese elemental map.

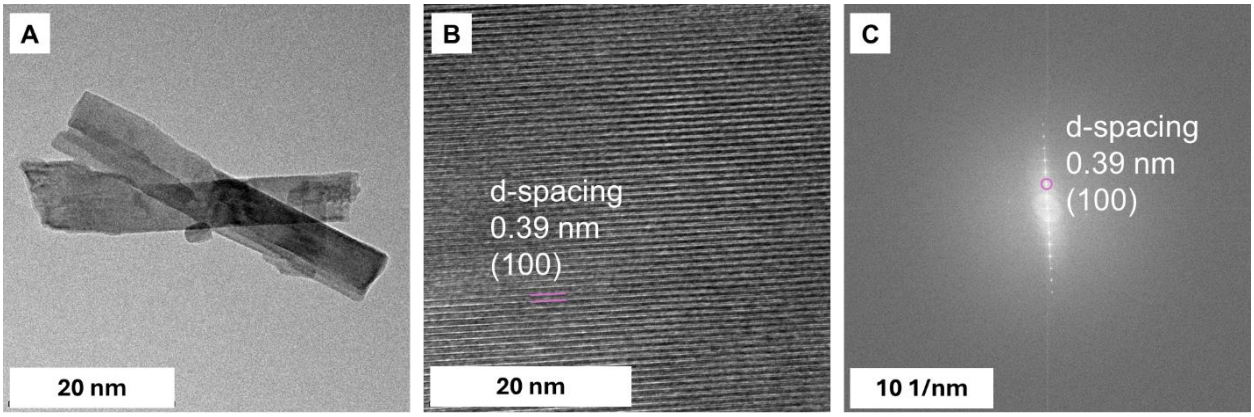

Figure S4. (A) TEM image of $MnSb_2O_4$ nanorods after treatment with a 1:1 molar ratio of XeF_2 in CH_3CN. (B) Lattice-resolved HRTEM image acquired for $MnSb_2O_4$ after treatment with a 1:1 molar ratio of XeF_2 indicating the separation between (100) planes. (C) Indexed SAED pattern acquired for indicating the (100) planes.

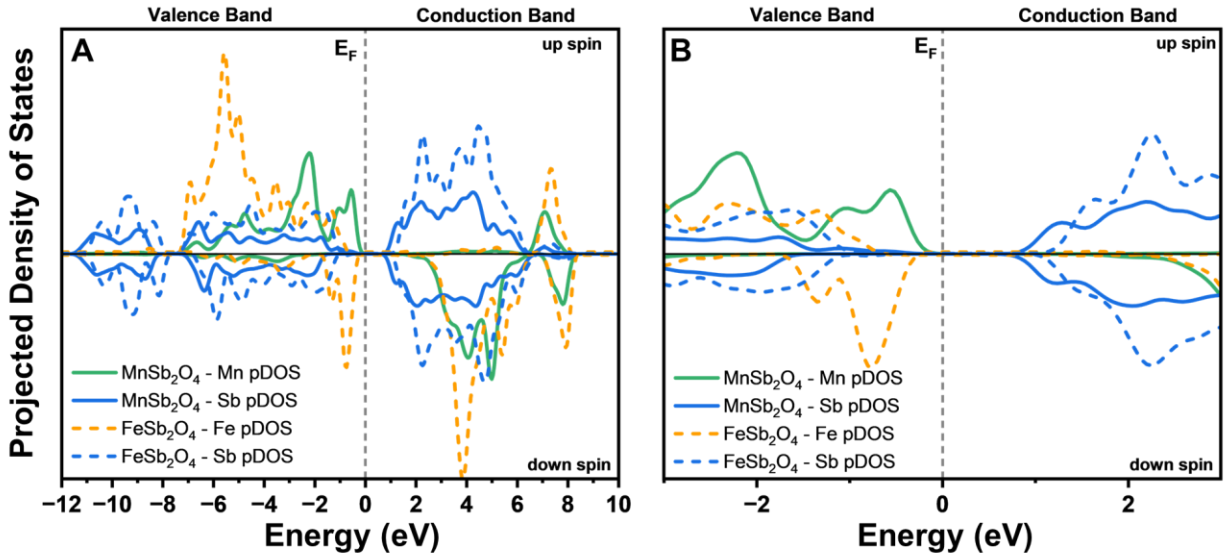

Figure S5. Comparison of transition metal and Sb projected density of states in $FeSb_2O_4$ and $MnSb_2O_4$ from (A) -12 to 10 eV and (B) -3 to 3 eV as a magnified view near the Fermi level.

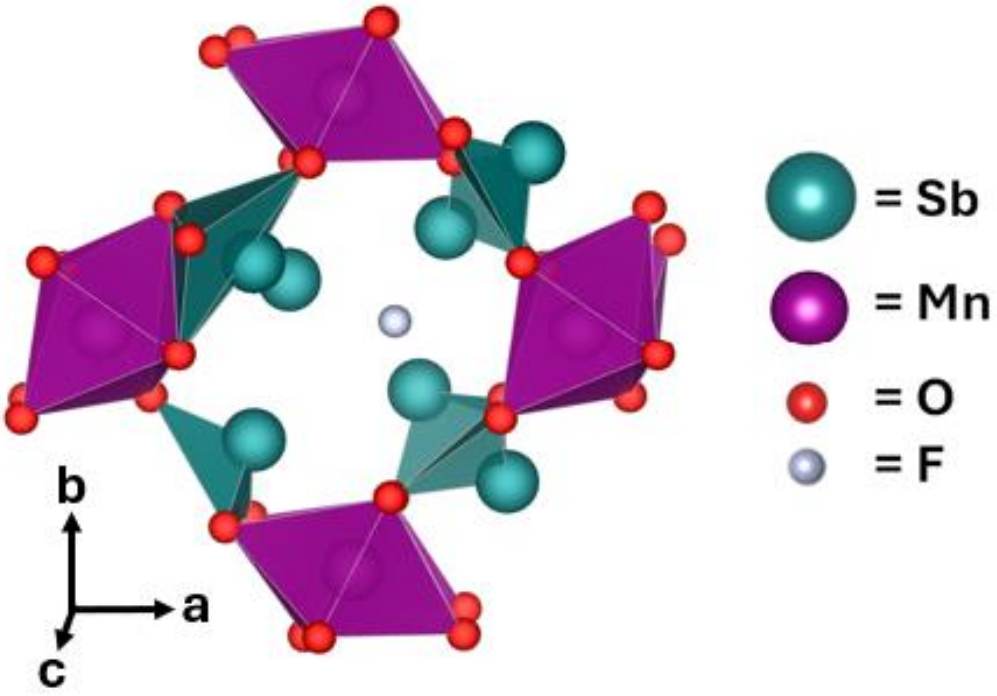

Figure S6. Putative optimized structure of $MnSb_2O_4F_x$ calculated via DFT methods seen along the crystallographic *c* direction.

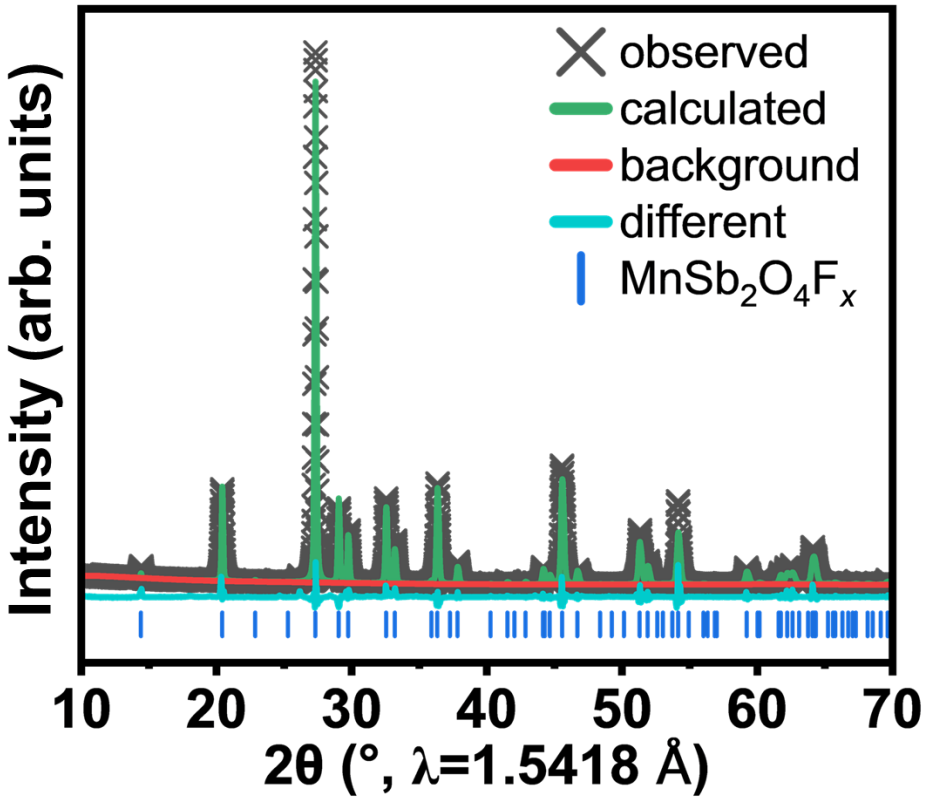

Figure S7. Rietveld refinement of powder diffraction data collected for $MnSb_2O_4$ after a 3 molar excess of $NOBF_4$ in CH_3CN. Refinement statistics, lattice parameters, and atom positions for the refinements of the reacted material are shown in Table S3.

Table S3. Atom positions, fractional occupancies, and thermal parameters obtained from Rietveld refinement of the powder XRD pattern acquired for $MnSb_2O_4$ after treatment with a 3 molar excess of $NOBF_4$ in CH_3CN. Refinement statistics and lattice parameters are included in the table header.

a = ***b*** = 8.69488 Å, ***c*** = 6.00444 Å ***α*** = ***β*** = ***γ*** = 90°; **Volume** = 453.942 Å^3 χ^2 = 64.497; R_{wp} = 16.698%; **RF** = 11.803%					
Atom Label	**Site Multiplicity**	***x***	***y***	***z***	**U_{iso}*100**
Mn	4	0.00	0.50	0.25	0.11(2)
Sb	8	0.1780(1)	0.1684(1)	0.00	0.01(0)
O(1)	8	0.0817(7)	0.6520(3)	0.00	0.22(5)
O(2)	8	0.6754(8)	0.1754(8)	0.25	2.84(1)
F	16	0.5273(5)	0.4961(7)	0.7404(2)	25

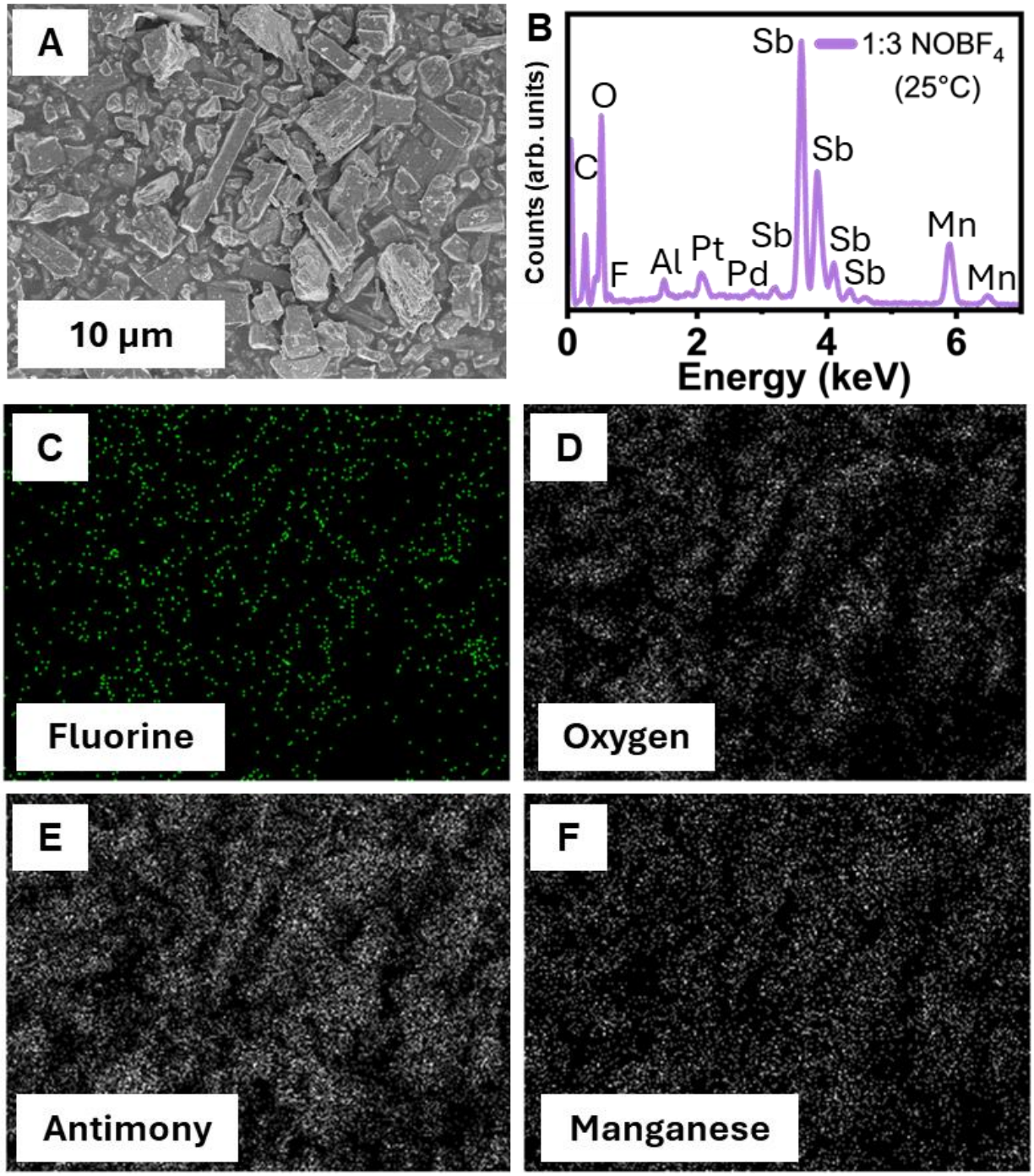

Figure S8. SEM-EDS images of 1:3 molar ratio of $NOBF_4$ in CH_3CN at 25 °C with (A) SEM image of as treated $MnSb_2O_4$; (B) EDS spectra; (C) fluorine elemental map; (D) oxygen elemental map; (E) antimony elemental map; and (G) manganese elemental map.

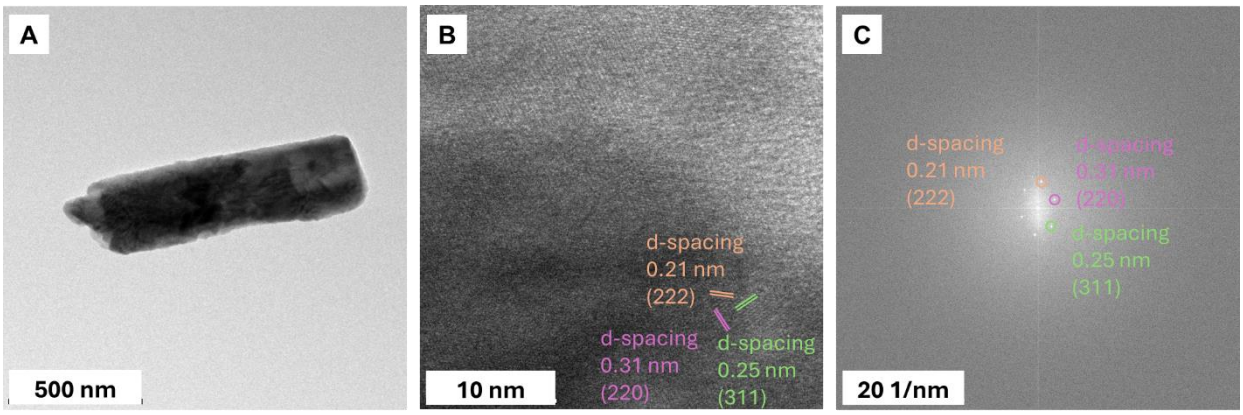

Figure S9. (A) TEM image of $MnSb_2O_4$ nanorods after treatment with a 3 molar excess of $NOBF_4$ in CH_3CN. (B) Lattice-resolved HRTEM image acquired for $MnSb_2O_4$ nanorods after treatment with a 3 molar excess of $NOBF_4$ in CH_3CN indicating the separation between (100), (220), and (311) planes. (C) Indexed SAED pattern acquired for indicating the (100), (220), and (311) planes.

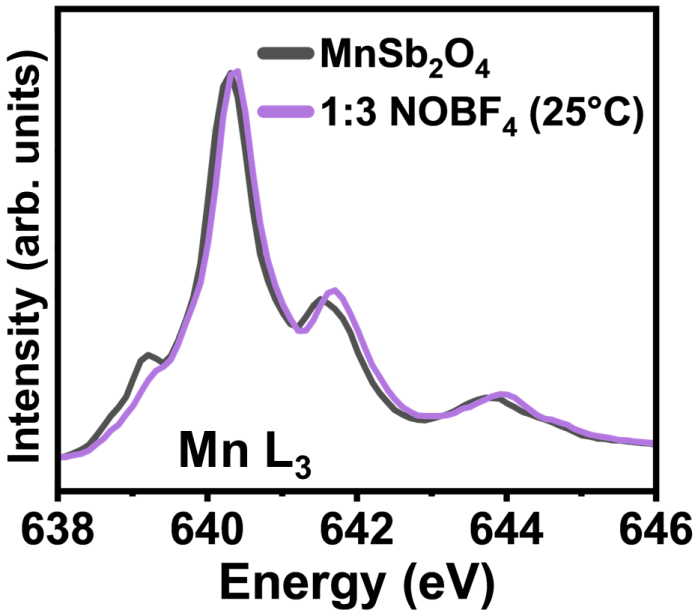

Figure S10. XANES Mn L_3-edge spectra for pristine $MnSb_2O_4$ and after treatment with a 3 molar excess of $NOBF_4$ in CH_3CN.

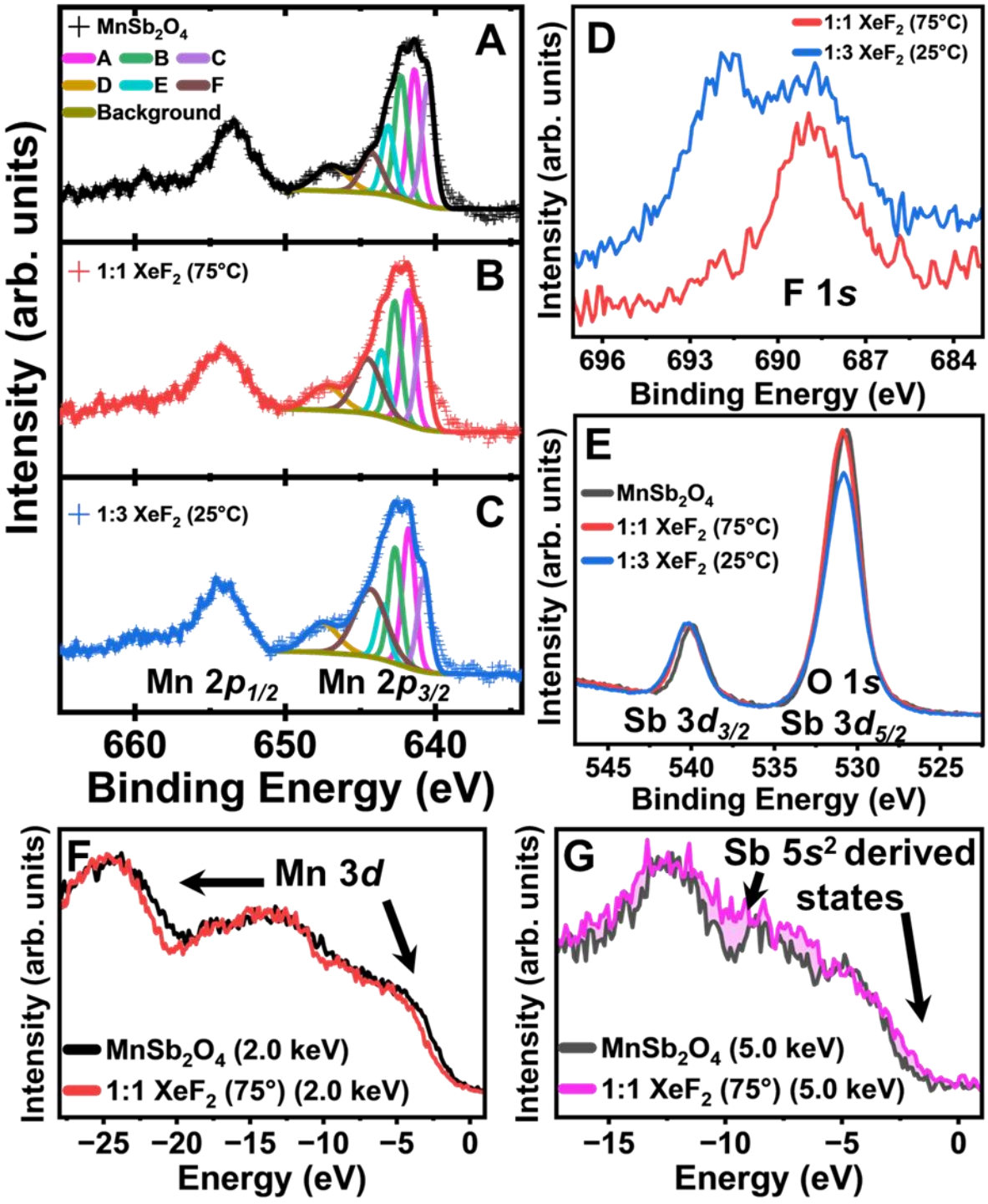

Figure S11. **Fluoridation Products upon Reaction with $NOBF_4$.** (A) XANES Sb M_4-edge and O K-edge spectra of as-prepared $MnSb_2O_4$ (gray) and after treatment with a 1:3 molar ratio of $NOBF_4$ (purple) in acetonitrile; (B) F-edge XANES spectra; (C) HAPXES F1s core level of $MnSb_2O_4$; (D) XPS spectra of $MnSb_2O_4$ (grey) and upon treatment with a 1:3 molar ratio of $NOBF_4$ (purple) in CH_3CN. Likely interphasic materials: (E) SbF_3, (F) SbOF, and (G) $Sb_2O_3F_5$.

Table S4. Possible reaction pathways for insertion and interphase formation: Products formed by the reaction of $MnSb_2O_4$ and XeF_2 in CH_3CN: (1) $MnSb_2O_4F_x$ (Insertion), (2) formation of MnF_2, (3) formation of MnF_3, (4) formation of SbF_3, (5) formation of SbOF, and (6) formation of $Sb_3O_2F_5$. Products formed by the reaction of $MnSb_2O_4$ and $NOBF_4$ in CH_3CN: (7) $MnSb_2O_4F_x$ (Insertion),

(8) formation of MnF_2, (9) formation of MnF_3, (10) formation of SbF_3, (11) formation of SbOF, and (12) formation of $Sb_3O_2F_5$. Each reaction was performed under flowing argon gas. Equation 9 depicts a potential interphase reaction; however, the balanced reaction requires oxygen gas as a reactant. Based on the greater density of argon gas versus oxygen gas, most likely oxygen was not present in the system. This reaction was included here for completeness.

$$\mathrm{MnSb_2O_4}(s) + \frac{\mathrm{x}}{2}\mathrm{XeF_2}(acetonitrile) \xrightarrow{24\ hrs} \mathrm{MnSb_2O_4F}_x(s) + \frac{\mathrm{x}}{2}\mathrm{Xe}(g) \quad \textbf{(1)}$$

$$2\mathrm{MnSb_2O_4}(s) + 2\mathrm{XeF_2}(acetonitrile) \rightarrow 2\mathrm{Xe(g)} + 2\mathrm{MnF_2}(s) + 2\mathrm{Sb_2O_3}(s) + \mathrm{O_2}(g) \quad \textbf{(2)}$$

$$2\mathrm{MnSb_2O_4}(s) + 3\mathrm{XeF_2}(acetonitrile) \rightarrow 3\mathrm{Xe(g)} + 2\mathrm{MnF_3}(s) + 2\mathrm{Sb_2O_3}(s) + \mathrm{O_2}(g) \quad \textbf{(3)}$$

$$2\mathrm{MnSb_2O_4}(s) + 6\mathrm{XeF_2}(acetonitrile) \rightarrow 6\mathrm{Xe(g)} + 2\mathrm{SbF_3}(s) + 2\mathrm{MnO}(s) + 3\mathrm{O_2}(g) \quad \textbf{(4)}$$

$$2\mathrm{MnSb_2O_4}(s) + 2\mathrm{XeF_2}(acetonitrile) \rightarrow 2\mathrm{Xe(g)} + 4\mathrm{SbOF}(s) + 2\mathrm{MnO}(s) + \mathrm{O_2}(g) \quad \textbf{(5)}$$

$$6\mathrm{MnSb_2O_4}(s) + 10\mathrm{XeF_2}(acetonitrile) \rightarrow 10\mathrm{Xe(g)} + 4\mathrm{Sb_3O_2F_5}(s) + 6\mathrm{MnO}(s) + 5\mathrm{O_2}(g) \quad \textbf{(6)}$$

$$\mathrm{MnSb_2O_4}(s) + x\mathrm{NOBF_4}(acetonitrile) \xrightarrow{24\ hrs} \mathrm{MnSb_2O_4F}_x(s) + x\mathrm{NO}(g) + x\mathrm{BF_3}(acetonitrile) \quad \textbf{(7)}$$

$$\mathrm{MnSb_2O_4}(s) + 2\mathrm{NOBF_4}(acetonitrile) \rightarrow \mathrm{MnF_2}(s) + \mathrm{Sb_2O_3}(s) + 2\mathrm{BF_3}(acetonitrile) + \mathrm{N_2O_3}(g) \quad \textbf{(8)}$$

$$\mathrm{MnSb_2O_4}(s) + 3\mathrm{NOBF_4}(acetonitrile) + \mathrm{O_2}(g) \rightarrow \mathrm{MnF_3}(s) + \mathrm{Sb_2O_3}(s) + 3\mathrm{BF_3}(acetonitrile) + 3\mathrm{NO_2}(g) \quad \textbf{(9)}$$

$$\mathrm{MnSb_2O_4}(s) + 6\mathrm{NOBF_4}(acetonitrile) \rightarrow \mathrm{MnO}(s) + 2\mathrm{SbF_3}(s) + 6\mathrm{BF_3}(acetonitrile) + 3\mathrm{N_2O_3}(g) \quad \textbf{(10)}$$

$$\mathrm{MnSb_2O_4}(s) + 2\mathrm{NOBF_4}(acetonitrile) \rightarrow \mathrm{MnO}(s) + 2\mathrm{SbOF}(s) + 2\mathrm{BF_3}(acetonitrile) + \mathrm{N_2O_3}(g) \quad \textbf{(11)}$$

$$3\mathrm{MnSb_2O_4}(s) + 10\mathrm{NOBF_4}(acetonitrile) \rightarrow 3\mathrm{MnO}(s) + 2\mathrm{Sb_3O_2F_5}(s) + 10\mathrm{BF_3}(acetonitrile) + \mathrm{N_2O_3}(g) \quad \textbf{(12)}$$

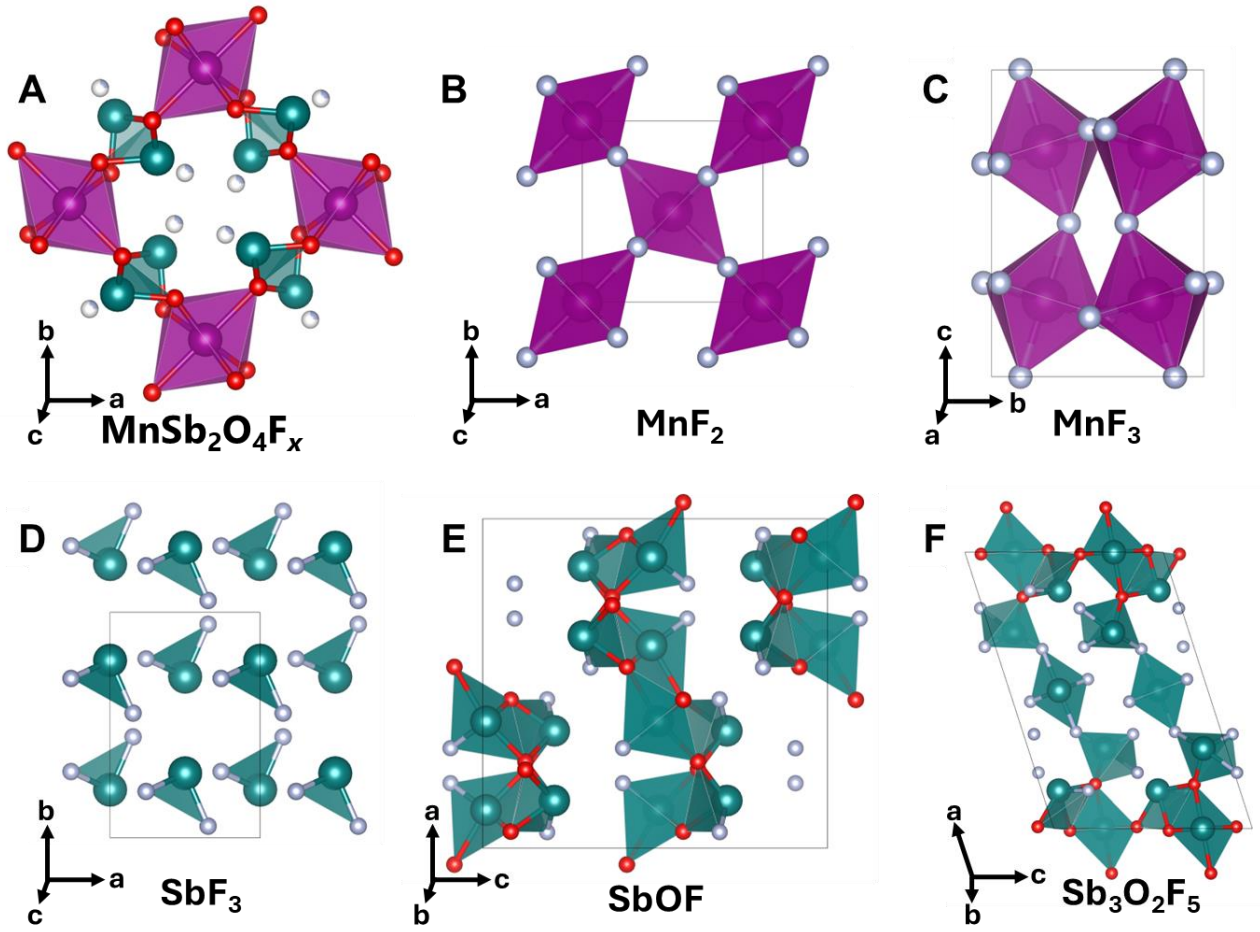

Figure S12. Potential reaction products after (A) insertion: $MnSb_2O_4F_x$; (B) manganese-based interphase formation: MnF_2; (C) manganese-based interphase formation: MnF_3; (D) antimony-based interphase formation: SbF_3; (E) antimony-based interphase formation: SbOF; and (F) antimony-based interphase formation: $Sb_3O_2F_5$.

Materials and Method

Synthesis of $MnSb_2O_4$ particles: 4 mL of a 0.334 mol/L $Mn(CH_3COO)_2{\cdot}4H_2O$ (≥99.999 %, VWR) aqueous solution was mixed with 4 mL of a 0.667 mol/L $SbCl_3$ (≥99.0 %, Millipore Sigma) aqueous solution prepared in 4 mol/L HCl (36.5% to 38.0%, Macron). The resulting mixture was titrated with 4 mL of an 8 mol/L aqueous solution of NaOH (≥98 %, Millipore Sigma) under constant stirring. The solution was then transferred to a polytetrafluoroethylene-lined high-temperature autoclave (Parr) and heated in a box furnace at 210 °C for 48 h. The autoclave was removed from heating and allowed to cool to room temperature autogenously. The solid product was separated from the supernatant by centrifugation and was washed twice with deionized water (8500 rpm for 10 min – Thermo Scientific Heraeus Megafuge 8)). The product was additionally washed (5×) by vortexing and then allowing the $MnSb_2O_4$ to settle (1—2 min) and decanted to remove the impurities based on density differences. A final centrifugation step was performed after dispersion in 2-propanol (VWR) (8500 rpm for 10 min). The product was dried at room temperature in air for 24 h and used without further modification for characterization and topochemical reactions.

Fluoridation of $MnSb_2O_4$ at 25 °C: Fluoridation reactions were performed in an argon-filled glovebox, maintained at O_2 and H_2O levels < 0.1 uL/L and 0.1 uL/L, respectively. A 35 mL aliquot of dry acetonitrile (< 50 uL/L H_2O, Millipore Sigma) was added to a 100 mL round bottom flask. 100 mg of as-prepared $MnSb_2O_4$ was added to the flask along with a five-fold molar excess amount of XeF_2 (listed as 1:5 XeF_2) (99.5 %, Thermo Fisher Scientific) at 25 °C. The mixture was stirred under argon for 24 h at 25° C. The excess acetonitrile was decanted and the obtained product was washed three times with 10 mL acetonitrile (Fischer Scientific)

and once with 10 mL 2-propanol. The powder was dried at room temperature in air. Additional fluoridation reactions were completed with a one molar ratio and a three-fold molar excess.

Fluoridation reactions of $MnSb_2O_4$ at high temperature: High-temperature fluoridation reactions were refluxed in dry acetonitrile at 55 °C for 24 h on a Schlenk line under an flowing Ar gas. The washing and drying procedure was the same as described for the sample fluoridated at 25 °C. Additional high-temperature reactions were completed at 75°C.

X-ray diffraction and structural characterization: Powder X-ray diffraction (XRD) patterns were collected in Brag-Brentano geometry on a Bruker D8-focus diffractometer (Cu K-α, λ = 1.5418 Å; 40 kV voltage; 25 mA current). All Rietveld refinements were performed using the EXPGUI user interface of GSAS-II.[1] Atomic positions, profile terms, lattice parameters, and inserted fluorine occupancies were refined from the laboratory XRD data using isotropic thermal parameters. All crystal structure renditions were prepared using the Vesta III software suite (JP-Minerals).[2]

XANES measurements: XANES measurements in partial electron yield (PEY) mode were performed at beamline 7-ID-1 of the National Synchrotron Light Source II of Brookhaven National Laboratory operated by the National Institute of Standards and Technology. A detector entrance grid bias of −300 V was used to reduce the low-energy electrons and improve the surface sensitivity. A charge compensation gun was used to avert the charging of the samples. The data were collected with a resolution of 0.2 eV and ≈0.3 eV at the O *K*-edge; and Mn *L*-, F *K*- and Fe *L*-edges; respectively. The PEY signals were normalized to the incident beam intensity using the photocurrent from a freshly evaporated gold mesh. The spectra were energy calibrated to the O K-edge for a standard TiO_2 sample.

Mn and Sb K-edge XANES spectroscopy measurements were performed under atmospheric conditions at beamline 7-BM, a bending magnet beamline of the National Synchrotron Light Source II of Brookhaven National Laboratory. The X-ray photon energy was monochromatized using a silicon (III) channel-cut crystal monochromator operating in continuous scan mode, Samples were prepared by uniformly spreading powder onto a piece of polyetherimide tape affixed to a sample holder designed for use at beamline 7-BM. 30 scans were performed at 30 s per scan and averaged to improve the signal-to-noise ratio. For the edges collected, before data acquisition, the beamline was calibrated by placing the corresponding elemental foil and measuring the edge position. Both transmittance fluorescence yield data were acquired in each case. Athena from the IFEFFIT package was used for data sanitization.

Hard X-ray photoemission spectroscopy: HAXPES measurements were performed at the National Institute of Standards and Technology beamline SST-2 of National Synchrotron Light Source II of the Brookhaven National Laboratory. Measurements at an incident photon energy of 2 keV were performed with a pass energy of 200 eV, whereas the measurements at an incident photon energy of 5 keV were collected with a pass energy of 500 eV. The data were collected with a step size of 0.85 eV, and the analyzer axis was oriented parallel to the photoelectron polarization vector. The higher excitation energy of HAXPES circumvents deleterious charging issues that are common to ultraviolet and soft X-ray photoelectron spectroscopy. Photon energy selection was accomplished by using a double Si(111) crystal monochromator. The beam energy was aligned to the Fermi level of a silver foil before measurements.

Scanning electron microscopy: SEM images were collected using a JEOL JSM-7500F FE-instrument, an ultrahigh-resolution field-emission scanning electron microscope (FE-SEM) equipped with a high brightness conical FE gun and a low aberration conical objective lens. $MnSb_2O_4$ powder was spread on conductive carbon tape and sputter coated with platinum before imaging. Elemental maps were collected using the JEOL JSM-7500F FE-instrument equipped with a high-brightness conical field-emission gun, a low aberration conical objective lens, and an Oxford energy dispersive spectroscopy (EDS) system.

Transmission electron microscopy: High-resolution transmission electron microscopy (HRTEM) images and selected area electron diffraction (SAED) patterns were acquired using a FEI Tecnai G2 F20 field emission scanning electron microscope (FE-TEM) operated at 200 kV. Prior to imaging, the powder samples were dispersed in 2-propanol and drop-cast onto 300-mesh formvar-carbon films supported by copper grids (electron microscopy science). HRTEM images were analyzed using the Gatan Microscopy Suite software.

Density Functional Theory Calculations: Geometry optimizations were carried out using DFT as implemented in the Vienna Ab-initio Simulation Package (VASP) for $MnSb_2O_4$.[3,4] Brillouin zone integration was performed using a 4×4×2 Monkhorst—Pack mesh.[5] The projector-augmented wave formalism was used to capture electron—ion interactions. Electron exchange and correlation were

addressed using the generalized gradient approximation based on the Perdew-Burke-Ernzerhof functional (PAW-GGA-PBE).[6–8] A Hubbard correction of U = 5.0 eV was used to account for strong electron correlation in the Mn 3d electrons as benchmarked in a previous study.[9] Electronic self-consistent loop and ionic relaxation loops were adjusted to be below 10^{-5} and 10^{-4} eV, respectively.

A single-point energy calculation was performed to calculate the projected density of state (pDOS) with Local Orbital Suite Toward Electronic-Structure Reconstruction (LOBSTER).[10,11] Bunge's description for the local basis functions were used for the pDOS calculation with 4*s* and 3*d* orbitals for manganese, 2*s* and 2*p* orbitals for oxygen, and 5*s* and 5*p* orbitals for antimony. The absolute charge spilling is lower than 1.26% in all cases.

Commercial names are mentioned in this paper to adequately specify the experimental procedure, and such specification is not intended to imply recommendation or endorsement by the National Institute of Standards and Technology.

Supporting References

(1) Toby, B.; Expgui, ¯. A Graphical User Interface for GSAS. *J Appl Cryst 210±213 J.* **2001**, *34*, 210–213. https://doi.org/10.1107/S0021889801002242.

(2) Momma, K.; Izumi, F. VESTA 3 for Three-Dimensional Visualization of Crystal, Volumetric and Morphology Data. *J. Appl. Crystallogr.* **2011**, *44* (6), 1272–1276. https://doi.org/10.1107/S0021889811038970.

(3) Kresse, G.; Hafner, J. Ab Initio Molecular Dynamics for Open-Shell Transition Metals. *Phys. Rev. B* **1993**, *48* (17), 13115–13118. https://doi.org/10.1103/PhysRevB.48.13115.

(4) Kresse, G.; Furthmüller, J. Efficient Iterative Schemes for Ab Initio Total-Energy Calculations Using a Plane-Wave Basis Set. *Phys. Rev. B* **1996**, *54* (16), 11169–11186. https://doi.org/10.1103/PhysRevB.54.11169.

(5) Monkhorst, H. J.; Pack, J. D. Special Points for Brillouin-Zone Integrations. *Phys. Rev. B* **1976**, *13* (12), 5188–5192. https://doi.org/10.1103/PhysRevB.13.5188.

(6) Blöchl, P. E. Projector Augmented-Wave Method. *Phys. Rev. B* **1994**, *50* (24), 17953–17979. https://doi.org/10.1103/PhysRevB.50.17953.

(7) Kresse, G.; Joubert, D. From Ultrasoft Pseudopotentials to the Projector Augmented-Wave Method. *Phys. Rev. B* **1999**, *59* (3), 1758–1775. https://doi.org/10.1103/PhysRevB.59.1758.

(8) Perdew, J. P.; Burke, K.; Ernzerhof, M. Generalized Gradient Approximation Made Simple. *Phys. Rev. Lett.* **1996**, *77* (18), 3865–3868. https://doi.org/10.1103/PhysRevLett.77.3865.

(9) Tolba, S. A.; Gameel, K. M.; Ali, B. A.; Almossalami, H. A.; Allam, N. K. The DFT+U: Approaches, Accuracy, and Applications. In *Density Functional Calculations - Recent Progresses of Theory and Application*; InTech, 2018. https://doi.org/10.5772/intechopen.72020.

(10) Maintz, S.; Deringer, V. L.; Tchougréeff, A. L.; Dronskowski, R. LOBSTER: A Tool to Extract Chemical Bonding from Plane-Wave Based DFT. *J. Comput. Chem.* **2016**, *37* (11), 1030–1035. https://doi.org/10.1002/jcc.24300.

(11) Nelson, C. T.; Winchester, B.; Zhang, Y.; Kim, S.-J.; Melville, A.; Adamo, C.; Folkman, C. M.; Baek, S.-H.; Eom, C.-B.; Schlom, D. G.; Chen, L.-Q.; Pan, X. Spontaneous Vortex Nanodomain Arrays at Ferroelectric Heterointerfaces. *Nano Lett.* **2011**, *11* (2), 828–834. https://doi.org/10.1021/nl1041808.